water

MDPI

Article

Mapping Complex Artificial Levees and Predicting Their Condition Using Machine Learning-Integrated Electrical Resistivity Tomography

Diaa Sheishah [1,2,*], Enas Abdelsamei [1,2], Viktória Blanka-Végi [1], Dávid Filyó [1], Gergő Magyar [1], Ahmed Mohsen [3,4], Alexandru Hegyi [5], Abbas M. Abbas [2], Csaba Tóth [6], Tibor Borza [7], Péter Kozák [7], Alexandru Onaca [5], Sándor Hajdú [1] and György Sipos [1,*]

1 Department of Physical and Environmental Geography, University of Szeged, Egyetem u. 2-6., 6722 Szeged, Hungary; enas.mohammed@nriag.sci.eg (E.A.); blankav@geo.u-szeged.hu (V.B.-V.); filyodavid852@gmail.com (D.F.); magyar.gergo94@gmail.com (G.M.); hajdusandor88@gmail.com (S.H.)
2 National Research Institute of Astronomy and Geophysics, El Marsad St., Helwan, Cairo 11421, Egypt; drabbasali@gmail.com
3 Department of Hydraulic and Water Resources Engineering, Faculty of Civil Engineering, Budapest University of Technology and Economics, Muegyetem Rakpart 3, 1111 Budapest, Hungary; ahmed_mohsen250@f-eng.tanta.edu.eg
4 Department of Irrigation and Hydraulics Engineering, Tanta University, Tanta 31512, Egypt
5 Applied Geomorphology and Interdisciplinary Research Centre (CGACI), Department of Geography, West University of Timisoara, 300223 Timisoara, Romania; alexandru.hegyi@e-uvt.ro (A.H.); alexandru.onaca@e-uvt.ro (A.O.)
6 Department of Highway and Railway Engineering, Budapest University of Technology and Economics, Műegyetem Rakpart 3., 1111 Budapest, Hungary; toth.csaba@emk.bme.hu
7 Lower Tisza District Water Directorate, Stefánia 4., 6720 Szeged, Hungary; borzat@ativizig.hu (T.B.); kozakp@ativizig.hu (P.K.)
* Correspondence: geo_diaa@nriag.sci.eg (D.S.); gysipos@geo.u-szeged.hu (G.S.)

Abstract

Artificial levees along major rivers are critical for flood-risk mitigation, yet many aging structures have poorly constrained internal composition and material heterogeneity, limiting the reliability of conventional safety assessments. This study develops a quantitative, non-destructive framework for characterizing levee internal structure by integrating electrical resistivity tomography (ERT) with borehole (BH) observations. ERT profiles were combined with borehole measurements of grain size (D50) and water content to investigate subsurface compositional variability and to evaluate relationships between sedimentological and geophysical parameters. Grain-size data from borehole samples were modeled using four predictive approaches—random forest regression (RFR), artificial neural networks (ANN), linear regression (LR), and support vector regression (SVR)—based on ERT-derived resistivity and moisture information. The results reveal pronounced internal heterogeneity within the investigated levees and demonstrate consistent relationships between sediment composition, water content, and electrical resistivity. Among the tested models, the ensemble-based RFR provided the highest predictive performance (R^2 = 0.81). These findings indicate that D50 characteristics of levee materials can be reliably inferred from ERT data using machine learning, reducing the need for destructive sampling. The proposed approach offers a transferable methodology for levee assessment and supports future applications in non-destructive monitoring, spatially explicit flood-risk analysis, and climate-resilient flood-protection management.

Check for updates

Academic Editor: Cesar Andrade

Received: 5 March 2026
Revised: 17 March 2026
Accepted: 26 March 2026
Published: 30 March 2026

Copyright: © 2026 by the authors. Licensee MDPI, Basel, Switzerland. This article is an open access article distributed under the terms and conditions of the Creative Commons Attribution (CC BY) license.

Keywords: alluvial rivers; levees; flood risks; electrical resistivity tomography; machine-learning algorithms; physical properties

1. Introduction

Floods are among the most widespread natural disasters, accounting for approximately half of all catastrophes in 2018. Besides the loss of human lives, floods significantly harm the economic and social infrastructure of affected regions [1,2]. One of the primary strategies for reducing flood risk is the construction of artificial levees along alluvial rivers. Although such levees have been constructed since antiquity, extensive large-scale endeavors have only commenced around the turn of the 20th century [3,4], utilizing diverse techniques and materials [5,6].

In the Carpathian Basin, the levee system provides safety for millions of inhabitants and hundreds of thousands of houses and thousands of km of roads and railways. The majority of the initial levees along the Tisza River and one of its main tributaries, including the Maros River, were constructed within a relatively short timeframe with insufficient height. Eventually, the levees evolved into complex earth structures resembling the layers of an onion, characterized by spatially variable compositions [7–9] subjected to various post-constructional processes, including compaction, subsidence, and water seepage during flood events [7,10,11]. Due to the cumulative impact of these processes (coupled with the historical evolution of the levees), comprehensive information regarding their structures and compositions is limited, posing significant challenges to flood-risk assessments and preparedness [12].

In this regard, electrical resistivity tomography (ERT), combined with geotechnical assessments, has proven to be a valuable tool for assessing levee conditions and the flood protection capabilities of levee sections [12–23]. In related research, Sentenac et al. [24] identified fissures in levees by using two- (2D) and three-dimensional (3D) ERT, while Fargier et al. [25] applied a 3D-extended ERT normalization approach to levee assessments. In order to control the seepage-water saturation and evolution of earth levees, Tresoldi et al. [26] conducted an ERT-based monitoring study of the levees in pseudo-real time. Specifically, they analyzed the influences of external variables such as temperature, water levels in the canal, and rainfall events on the resistivity data at different depths of the levee body during different time periods. The geophysical surveys can also be complemented by geotechnical investigations [27,28]. In related studies, Jodry et al. [29] monitored the seasonal soil-moisture changes and temperature profiles in an earthen levee by using 2D direct-current ERT, and generated seasonal resistivity-change models, while Rahimi et al. [30] combined capacitively coupled resistivity with a multichannel analysis of surface waves to map the near-surface structures of the Melvin Price Reach of the Wood River Levee. Subsequently, Sheishah et al. [6] identified the potential problem areas along various levee sections in Hungary. Geophysical methods like ERT and GPR effectively assess levee integrity and identify seepage pathways. A controlled experiment validated their reliability, highlighting their utility for flood risk assessment in areas with undocumented levee construction [23].

Many authors used different machine learning (ML) algorithms to predict different soil properties. Padhan et al. [31] and Bordas et al. [32] used neural networks (CNNs) to guess how the grain sizes would be spread out based on various microstructural features. Ding and El-Zein [33] used data from the UNSODA database to study how artificial neural networks (ANNs) could be used to guess soil water retention curves (SWRCs). Bordignon et al. [34] used 3D convolutional neural networks to figure out the grain size and porosity

distributions from 3D grayscale microtomography images. They did this to circumvent the high cost of employing humans and computers to separate the images and determine these properties. Hamada et al. [35], applied ANN to predict porosity and water saturation in shaly sand reservoirs. Sastre et al. [36] propose an automatic methodology to predict the soil grade based on the cone resistance using ANN. Kundu et al. [37] did a full study on how machine learning can be used to predict electrical resistivity (ER) in different types of soil. They created three predictive models: Support Vector Regression (SVR), ANN, and Extreme Gradient Boosting (XGB). The authors conducted 2772 ER tests across seven different soil types, considering multiple input parameters such as temperature, density, and moisture content, which are crucial for accurate resistivity predictions. Traditional methods often relied on single input variables, but this study emphasizes the importance of multiple parameters due to their combined effects on resistivity. Chang et al. [38] and others used machine learning and resistivity measurements to make a detailed 3D Apparent Geological Model (AGM). They did this because there was a link between resistivity values and the types of sediment found in nearby boreholes. Using the Random Forest Regressor (RF) algorithm to connect resistivity data with different types of sediment found in boreholes, three types of sediment were found: gravel (>140 Ohm-m), sand (60–140 Ohm-m), and clay (<60 Ohm-m). These studies highlight the growing use of ML in geotechnical contexts. However, most prior work focuses on either image-based grain sizing or predicting soil behavior from databases, with relatively few studies integrating field geophysical measurements with ML for levee evaluation.

Conventional procedures for assessing levee materials frequently depend on destructive methods to ascertain grain size (D50), which are challenging, resource-demanding, and restricted in spatial extent. Modern geophysical investigations, while encouraging, frequently exhibit insufficient integration of resistivity data with water content measurements to accurately forecast grain size.

There is still limited application of machine learning in developing models capable of accurately predicting the median grain size (D_{50}) of levee materials. Consequently, fast, non-destructive, and scalable methods for levee material characterization remain scarce. Moreover, only a few studies have focused on in situ characterization of levee materials using machine learning, particularly those that aim to predict grain size (D_{50}) directly from geophysical measurements and soil moisture data.

This research mitigates this gap to improve the efficiency and precision of grain size prediction in levee systems. Therefore, this study aims to integrate ERT method, BH data, and machine learning to (1) map the structural and compositional complexities of two levee systems and analyze their implications for flood protection challenges, (2) improve the accuracy of correlations between water content and other physical parameters of borehole samples, and (3) increase reliance on non-destructive geophysical techniques for estimating the grain size (D50) of levee materials, reducing dependence on traditional destructive methods.

In order to achieve these aims the following objectives are as follow; (1) identify and compare structural and compositional differences between the two levee systems and evaluate how these differences may influence flood protection performance, (2) develop and refine a classification method for borehole samples based on their water content, enabling more meaningful correlations between water content and other physical parameters, and (3) build predictive machine learning models that estimate the grain size (D50) of levee materials using measured resistivity and water content, facilitating rapid and accurate evaluations over extended sections.

2. Study Area

Artificial levees were built more than 150 years ago, as part of the flood-risk protection measures for floodplains in the Carpathian Basin. Meanwhile, flood hazard maps in Hungary, which are accessible online (OVF, 2015), provide information on the areas protected from floods. In fact, the 20th and 21st centuries have been marked by increases in peak flow levels, particularly in the dynamic fluvial system of the Tisza River [39].

Regarding the study area, it is situated on the left banks of the Tisza and Maros Rivers in the southern part of Hungary. Geophysical surveys and drillings were performed along a 48-km levee section (Figure 1). The investigated levees were last reinforced in the 1970s, but their internal structures and layer compositions have yet to be fully understood. The precise structure and composition of the levees are only known along newly constructed sections, since such works in the 19th century were rarely documented. Furthermore, since reinforcements are made from nearby materials, the vertical and horizontal compositions of the levees are highly heterogeneous. Hence, these structural and compositional changes must be mapped for future flood management [6,40].

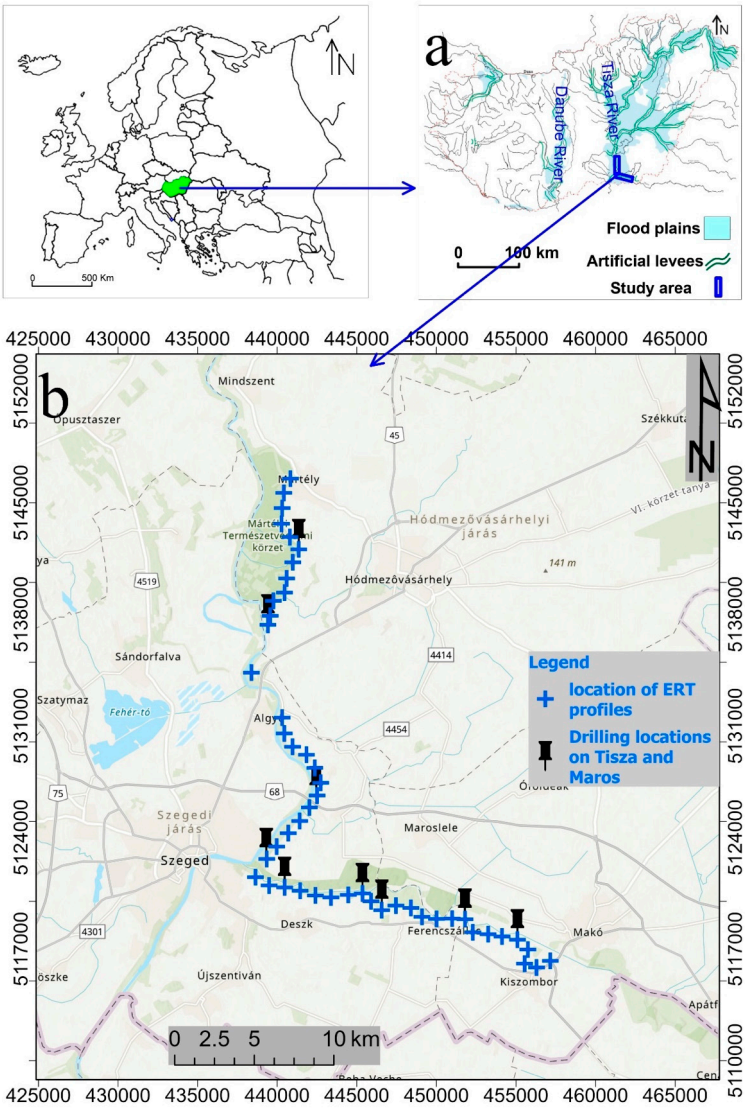


Figure 1. (**a**) Location map of potential floodplains and artificial levees in Hungary (modified from OVF—General Directorate of Water Management, Hungary [41]) and (**b**) Study area in southern Hungary showing the ERT monitoring profiles and drilling locations along the Tisza and Maros Rivers

(lkm = levee kilometre, a standardized river engineering unit indicating distance along the levee alignment). The location map in panel (**b**) was prepared using ArcGIS Pro, and the basemap (World Topographic Map) displays place names in their original Hungarian form. These names are retained as official geographic identifiers; translating them into English would result in non-standard and potentially misleading place names.

3. Data and Methods

3.1. ERT Measurements

In the present study, the ERT profiles along the investigated levee sections were collected by using a Wenner array and a GeoTom MK8E100 apparatus with a 50-electrode system. A total of 109 ERT profiles were collected at two levee sections: (1) the left bank of the Tisza River, from 13 to 42 lkm; and (2) the left bank of the Maros River, from 1 to 24 lkm. All ERT measurements were conducted during the same field campaign period under stable hydrological conditions, avoiding flood events and prolonged precipitation periods. This ensured that seasonal variations in soil moisture did not significantly affect the comparability of the profiles. In addition, in situ water-content measurements obtained from borehole samples were incorporated into the analysis to explicitly account for the influence of moisture on electrical resistivity (R). Since the composition of the levee core can differ in each side (as well as throughout the core structure), two profiles were measured at each lkm in the investigated sections. The first profile was measured longitudinally on the levee crown, while the second profile was measured transversely across the levee crown and both sides (i.e., the river and protected sides) of the levee. In this case, the transverse profile was topographically corrected by using the elevation data at each odd-numbered electrode along the survey line, acquired by a real time kinematic global positioning system (RTK GPS) (TopCon Hyper Pro) [40].

Overall, 61 ERT profiles along the Tisza levee were measured from 13 to 24 lkm and from 31.4 to 42 lkm. The 25–30 lkm section was omitted because the levee crown is paved. At 28 lkm, the longitudinal ERT profile was measured, but the transverse profile was omitted because the levee crown is crossed by road traffic. During the preliminary ERT measurements, one cable was connected to the 25-electrode control unit. In this case, the longitudinal profiles (92 data points; eight data levels; and 60 m profile length) were obtained at an electrode spacing of 2.5 m. Meanwhile, the transverse profiles (92 data points; eight data levels; and 48 m profile length) were obtained at a shorter electrode spacing (2.0 m) because the profile length covered the entire levee width (crown and both sides) in some sections. The transverse profiles were adjusted after that because the width in some sections of the levee exceeded that of the previous investigated section. Hence, the transverse profiles (392 data points; 16 data levels; and 73.5 m total length) were collected by using two 50-electrode cables with an electrode spacing of 1.5 m.

A total of 48 ERT profiles along the Maros levee were measured at 1-lkm intervals, from 1 to 24 lkm. The profile lengths, total numbers of data points and data levels, electrode numbers, and electrode spacing of the longitudinal and transverse profiles were as described earlier for the Tisza levee [40].

To obtain the true resistivities of the building materials of the levees, the resistivity values obtained during the ERT profiling were processed by using RES2DINV 3.4 software [42]. Before initiating the inversion process, we removed the noisy outlying data points. The inversion scheme was based on the least-squares smoothness-constrained iterative optimization algorithm [43,44]. In this case, inversion was preceded by topographic adjustment in order to remove the elevation effect from the transverse profiles. Moreover, when the root-mean-square values were sufficiently low, the inverted ERT profiles were exported for evaluation.

3.2. Sedimentological Data

The borehole drillings and sediment sampling were conducted during the same field campaign as the ERT measurements to ensure temporal consistency between the geophysical and sedimentological datasets. This synchronization minimized potential deviations caused by temporal changes in soil moisture or environmental conditions. To accurately interpret and validate the ERT surveys, 19 boreholes were drilled at 13, 18, 31.4, and 37 lkm along the Tisza levee and at 3, 8, 10, 16, and 20 lkm along the Maros levee. At each site, one borehole, with a depth of 6–7 m, was drilled on the riverside edge of the levee crown, while a second borehole, with a depth of 3–4 m, was drilled on the protected side slope of the levee. The 19th borehole was drilled at a depth of 2 m on the levee foot of the 16 lkm site. Drilling was carried out by using an Eijkelkamp drilling system with a 5-cm diameter drilling head [40].

Meanwhile, samples were collected at 20-cm depth intervals for median grain size (D50) analysis by using a Fritsch Analysette 22 laser analyzer, with a measurement range of 0.08–2000 μm. The samples (200 and 255 from the levees of Tisza and Maros Rivers, respectively) were completely dried in a drying oven at 105 °C and ultrasonically homogenized in the laboratory, with their D50s measured three times to check for further disintegration. To ensure measurement reliability, replicate measurements were evaluated for consistency and the average value was used for further analysis. The ultrasonic dispersion and repeated measurements served as quality-control procedures to minimize particle aggregation and analytical variability. The D50 fractions of the samples were recorded on the Udden-Wentworth scale. In this study, the sample D50s were applied as controls of the geophysical results.

Another set of 220 drilling samples was collected for in situ water content (W) measurements at 40-cm intervals during the drilling procedure. These samples were stored in special plastic bags and their wet weights were measured before being dried in a drying oven at 100 °C in the laboratory. The weights of the dried samples were then measured and subtracted from the wet weights to determine the W (as a percentage).

The other physical parameters of the levee composition, such as density (ρ), porosity (φ), and saturated hydraulic conductivity (K), were determined from 49 samples collected in soil-sample rings during the borehole drillings. The samples were collected at depths with obvious stratigraphical changes. After measuring their Ks with a penetrometer, the samples were dried in a drying oven and weighed in the laboratory.

The dry bulk density was obtained as the dry weight of each sample divided by the volume of the soil-sampling cylinder. The total porosity (%) was then calculated as follows:

$$\varphi = 100\,[1 - \frac{\rho b}{\rho d}] \quad (1)$$

where ρb and ρd are the bulk and particle densities of the material (g/cm^3), respectively. Following Fetter [45], the particle density was taken as 2.65 g/cm^3. Fetter [44] also reported that the porosity will decrease if a sediment contains mixed grain sizes because the smaller particles will fill the voids between the larger particles. Since the grains in the artificial levees of the Tisza River showed no large variations, the porosities of the samples were high. As for the parameter correlations and their significance degrees, they were determined by using IBM SPSS version 26, a powerful and user-friendly software package for statistical data analyses [46]. As the correlation methods, we selected the Pearson and Spearman methods.

Overall, the resistivity (R) determined from the ERT profiles of the 49 samples collected from the 10 different boreholes was correlated with W, D50, K, φ, and ρ. Some values of K and φ are not reported in Table A1 because reliable laboratory measurements could not be

obtained for a small number of samples. In a few cases, the collected sediment samples were insufficient in volume or were disturbed during sampling and therefore could not be reliably analyzed in the laboratory. These cases represent only a minor fraction of the dataset and do not influence the overall interpretation of the results.To better understand how moisture influences the resistivity-grain size relationship, W measurements were binned into three ranges: Class 1 = dry (W 0–10%), Class 2 = intermediate moisture (W 11–20%), and Class 3 = high moisture (W $\geq$ 21%). We then examined R–D50 correlations within each W class.

3.3. Machine-Learning Method

In this study, different ML algorithms, e.g., RFR, ANN, LR, and SVR were used to predict the dependent variable (D50) from the independent variables (W and R). The selected machine-learning algorithms represent complementary modeling approaches with increasing complexity. LR provides a baseline linear reference, SVR and ANN capture non-linear relationships, and RFR offers robust ensemble learning with strong generalization and physical interpretability, enabling a systematic comparison of predictive performance for D50 estimation.

The dataset was split into 80% for training and 20% for testing, and the Grid Search CV algorithm was used to fine-tune the model's hyperparameters.

The RF was proposed by [47]. The basis of RF is the decision tree (DT) algorithm, as the RF comprises multiple DTs operating concurrently. The RF method involves partitioning the input data features into DTs. Subsequently, each tree provides its forecast based on the incorporated attributes, and the ultimate prediction of the RF is the average of all decision trees' outcomes. The RF mitigates overfitting, which could give rise to a solitary DT; additionally, it can improve the model's accuracy. Many hyperparameters can be changed to achieve the optimal performance of the RF model, such as the number of estimators, the maximum feature, minimum sample split, and minimum sample leaf. Our work employed the RFR module in the scikit-learn library in Python version 3.11 to develop the RFR model for D50 prediction.

The ANN includes three layers: input layer, hidden layer, and output layer [48]. Each layer contains numerous cells (neurons), which receive a signal (impulse) from the preceding neuron and deliver their result after executing various changes onto the adjacent neuron. These neurons are interconnected by weights, which are initially assigned randomly at the commencement of the training process and subsequently modified at each iteration until optimal weights are attained [49]. The neural network from the scikit-learn module in Python was employed to construct the model. The rectified linear unit (ReLU) activation function, which regulates the weighted sum of inputs for transmission to the succeeding neuron, was utilized in the hidden layers. The "relu" function outputs the input value in all instances except when the input is zero, in which case it returns zero [f(x) = max (0, z)], so circumventing the saturation issue present in other activation functions like sigmoid and tanh. The limited memory Broyden–Fletcher–Goldfarb–Shanno (lbfgs) solver, which optimizes the weights of every neuron to minimize the cost function, was also applied to the hidden layers. The "lbfgs" updates weights by calculating the inverse of the Hessian matrix [50–53].

LR is a supervised learning approach that predicts the connection between a dependent variable and one or more independent variables by fitting a linear equation to the observed data. The model decreases the mean squared error (MSE) between anticipated and actual values by optimizing the coefficients (weights) through techniques such as ordinary least squares (OLS). The LR module of the scikit-learn toolkit in Python was employed for automatically calculating these coefficients. The above approach presupposes

a linear correlation, independence of errors, and homoscedasticity (unified variance of errors). The algorithm's simplicity and interpretability make it a core tool in predictive modeling programs.

The SVM generates the optimal hyperplane that intersects the highest number of data points. However, the fundamental distinction between the SVR and the other regression models is that these models strive to identify the best fit line, which minimizes the square error between the fitted line and points. At the same time, the SVR allows for a degree of tolerance in the solution, since it endeavors to identify the optimal fit line within a specified threshold value, so enhancing the probability of achieving superior solutions [54]. The kernel is tasked with identifying the hyperplane, particularly in high-dimensional space problems. This study uses the SVR in the scikit-learn module in Python to construct the SVR model for D50 prediction.

All settings and parameters used in these ML algorithms were applied following the fine-tuning of hyperparameters (Figure 2) to achieve optimal outcomes.

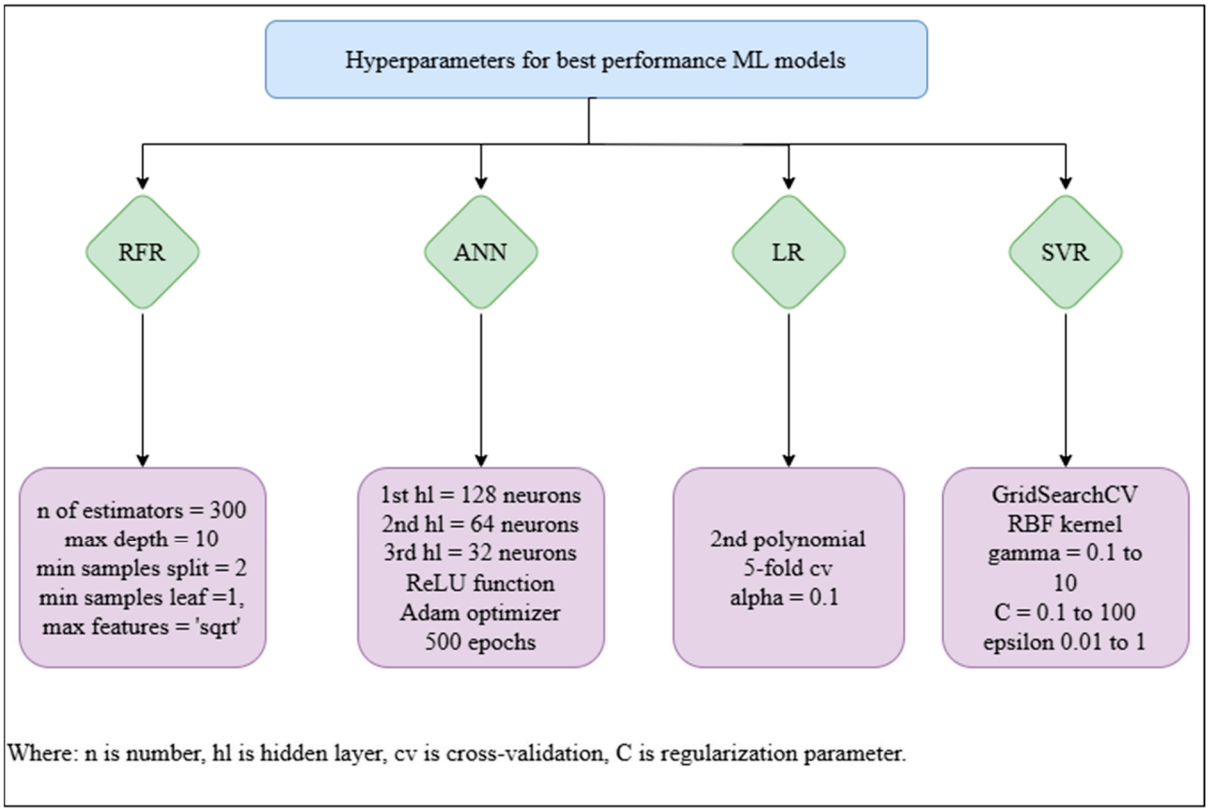


Figure 2. Schematic representation of the optimized hyperparameters used for the machine-learning models applied in this study. The figure summarizes the configurations that provided the best predictive performance for RFR, ANN, LR, and SVR models used to predict sediment D50 from R and W. The selected hyperparameters were determined through model tuning and cross-validation to ensure optimal model performance.

RFR hyper-parameters, including the number of estimators (trees in the forest), maximum tree depth, minimum samples to split a node, minimum samples at a leaf, and maximum number of features examined at each split, were optimized using grid search (Figure 2).

The ANN model was developed using TensorFlow Keras Sequential. Three hidden layers were utilized in the ANN model. The first hidden layer has 128 neurons, the second 64, and the third 32. All hidden layers applied ReLU activation, which handles non-linear relationships. To avoid overfitting, we added 20% dropout layers between concealed

layers. The Adam optimizer efficiently adjusted learning rate during model training. ReduceLROnPlateau, a learning rate scheduler, dynamically reduced the learning rate when validation loss plateaued, improving convergence across 500 epochs. Performance was improved by standardizing features with StandardScaler. Prior to model training, the input variables (R and W) were standardized to ensure that variables with different magnitudes contributed equally to model training. This step is particularly important for distance-based algorithms such as SVR and for ANN training. In addition, noisy or extreme geophysical measurements were filtered during the ERT inversion stage using quality-control procedures implemented in the RES2DINV software, which helped reduce the influence of measurement noise on the dataset used for machine-learning modeling. Second-degree polynomial features were utilized in the LR model to account for non-linear relationships and improve flexibility. Ridge regression, or LR with L2 regularization, was chosen to enhance model performance and reduce overfitting. Grid search with 5-fold cross-validation was applied to optimize alpha from 0.1 to 100. We also applied SVR model for complex trends like D50 distribution because it can capture non-linear correlations in data. We normalized the features using the StandardScaler before applying the SVR model to guarantee that all variables were on the same scale, which is necessary for distance-based models like SVR. We optimized model performance with GridSearch CV hyperparameter adjustment. The best hyper-parameters for the models used are explained in Figure 2.

The efficiency of the proposed models was assessed utilizing five statistical metrics: coefficient of determination (R^2), Root Mean Square Error (RMSE), Mean Absolute Percentage Error (MAPE), Median Absolute Error (MEDAE), and Mean Absolute Error (MAE) [55–58] as follow:

1. Coefficient of Determination (R^2) measures how well the regression model explains the variability of the dependent variable. It is calculated as:

$$R^2 = \frac{\left(\Sigma(a_i - \bar{a})\left(b_i - \bar{b}\right)\right)^2}{\Sigma(a_i - \bar{a})^2 \times \Sigma\left(b_i - \bar{b}\right)^2} \quad (2)$$

2. Root Mean Squared Error (RMSE) calculates the square root of the average squared differences between actual and predicted values. It is defined as:

$$RMSE = \frac{\sqrt{(\Sigma(a_i - b_i)^2)}}{n} \quad (3)$$

3. Mean Absolute Percentage Error (MAPE) expresses the prediction error as a percentage of actual values. It is given by:

$$MAPE = \left(\frac{1}{n}\right)\Sigma(|(a_i - b_i)/a_i|) \times 100 \quad (4)$$

4. Mean Absolute Error (MAE) computes the average absolute differences between actual and predicted values. It is defined as:

$$MAE = \left(\frac{1}{n}\right)\Sigma(|a_i - b_i|) \quad (5)$$

5. Median Absolute Error (MEDAE) calculates the median of absolute differences between actual and predicted values. It is defined as:

$$MEDAE = \text{median}(|a_i - b_i|) \quad (6)$$

where n is the number of data points, a_i is the observed value, b_i is the predicted value, $\bar{a}$ is the mean of the observed value, and $\bar{b}$ is the mean of the predicted value.

4. Results

4.1. Integrating ERT and Sedimentological Data to Identify Structural Units at Tisza and Maros Levees

The difference in the composition of the Tisza and Maros levees is visible in the resistivity results at the representative levee sections 18 lkm and 16 lkm of Tisza and Maros levees, respectively, because more drilling information and analysis are provided at the mentioned locations. In general, the inverted ERT profiles exhibited low resistivity values in the Tisza levee and medium and high values in the case of the Maros levee. The longitudinal and transverse profiles measured on the Tisza levee exhibited a range of values from 13.3 Ωm to 82.5 Ωm, averaging 28 Ωm. In the case of the longitudinal profile measured on the Maros levee, values ranged between 24 Ωm and 108 Ωm with an average of 65 Ωm. In the Transverse profile measured on the Maros levee, values were considerably higher, reaching a maximum of 3025 Ωm, and the mean specific resistivity was 1522 Ωm (Figure 3).

The extremely high resistivity values observed in the transverse profiles of the Maros levee (up to 3025 Ωm) are interpreted as coarse sand lenses characterized by low moisture content and high permeability. In unconsolidated sediments, electrical resistivity is primarily controlled by pore-water content, grain-size distribution, and pore structure. Coarse sands typically exhibit significantly higher resistivity values than fine-grained silts because of their lower clay content and reduced surface conduction. This interpretation is supported by the correlations observed in the borehole dataset, where resistivity increases with larger D50, higher φ, and higher K, while decreasing with increasing W.

The longitudinal profile measured at the investigated site of the Tisza levee exhibited one unit; this was the fine silt, which is the dominant component of the levee body, with resistivity values ranging between 6 Ωm and 29 Ωm (Figure 3A). A very fine silty layer, 0.4 m thick and at a depth of 4 m, could not be resolved on the ERT profile as it showed only minor accumulations and did not show a layered structure. The transverse profile measured at this zone exhibited the same unit with approximately the same resistivity range. In addition, a second unit of medium silt was noticed on both sides of the Tisza levee, with resistivity values ranging between 29 and 81 Ωm (Figure 3B). The protected side of the Tisza levee shows a main composition of fine silt at the drilling location at the bottom, while ERT could not resolve it.

The materials forming the Maros Levee differ from those in the Tisza Levee. Three successive units were identified in the longitudinal ERT profile measured on the crown of the Maros levee at 0–3 m, 3–4.5 m, and 4.5 m–bottom with average resistivity values 95 Ωm, 49 Ωm, and 28 Ωm which relate to medium and coarse, fine, and medium silts, respectively (Figure 3C).

The variation in Maros levee composition is even more visible, especially on the protected side where two big lenses of medium and coarse sands could be noticed. In addition to one lense of the same composition on the levee foot. Six units could be resolved; the first medium sandy unit with a thickness of ~0.4 m has an average resistivity 250 Ωm, the second medium silty unit with a thickness of ~0.5 m has an average resistivity 550 Ωm, the third unit in the form of a lense of medium and coarse sand with ~3 to 3.5 m thick has a high resistivity with an average 1500 Ωm, the fourth medium silty unit (~1 m thick) has an average resistivity 550 Ωm, the fifth medium sandy unit (~1 m thick) has an average resistivity 250 Ωm, and the last unit in the form of fine silt extended until the maximum depth reached by ERT with an average resistivity 60 Ωm. The levee foot shows a very

high resistivity unit of medium and coarse sand (~0.8 m thick) with an average resistivity 2200 Ωm, then a thin unit of coarse silt (~0.2 m thick) with an average resistivity 660 Ωm, and then a fine and medium silty unit with an average resistivity 340 Ωm (Figure 3D).

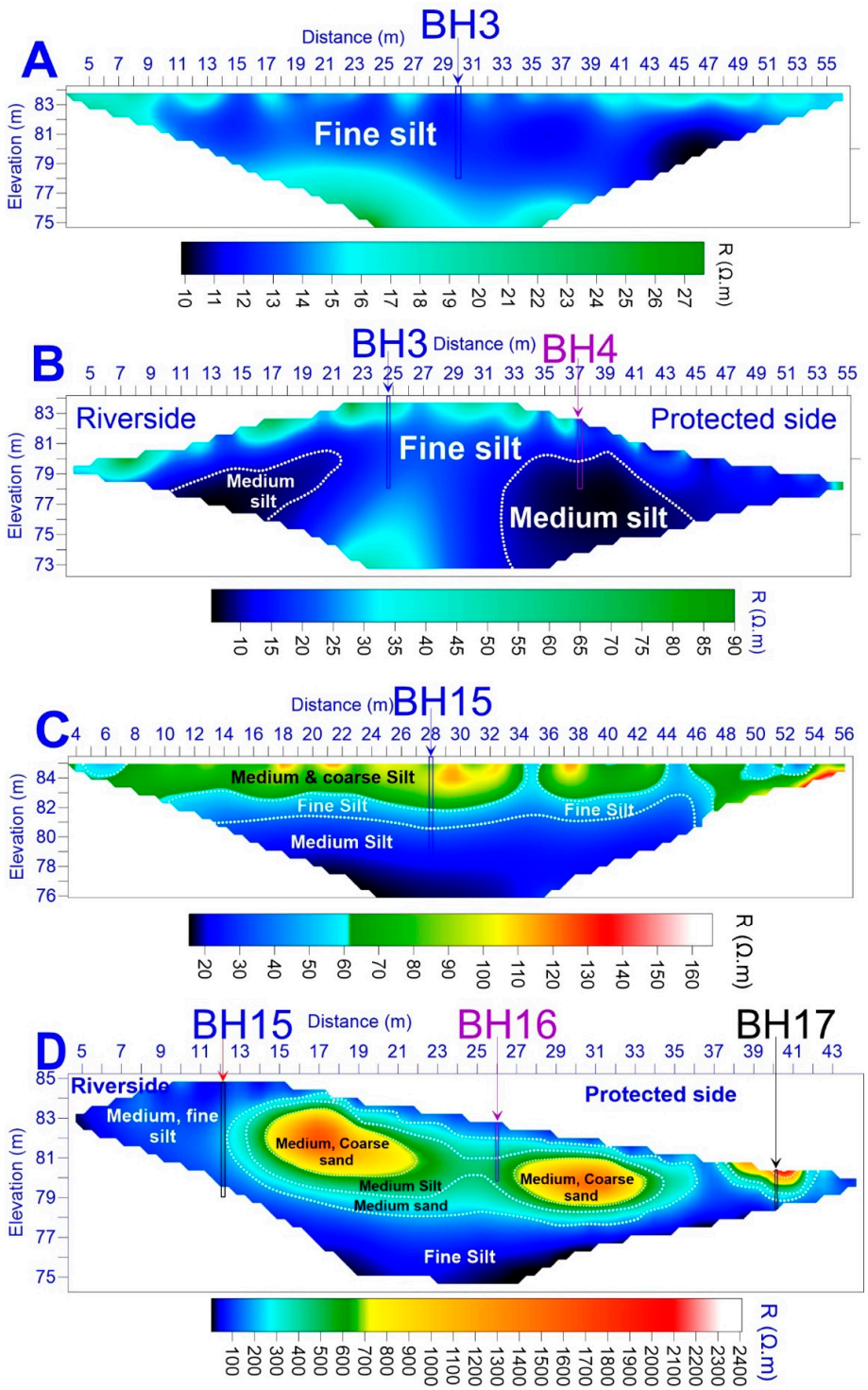


Figure 3. Samples of the inverted profiles: Longitudinal (**A**) and transversal (**B**) ERT profiles acquired on the Tisza levee at 18 lkm. Longitudinal (**C**) and transversal (**D**) ERT profiles acquired on the Maros levee at 16 lkm.

4.2. Mapping of Materials Along the Investigated Levees

Assisted by sedimentological data, the ERT revealed the structures and changes of the materials along the investigated levee sections. Specifically, along the Tisza levee section

and following the longitudinal profiles measured on the Tisza levee crown, the levee core was dominated by two materials: medium and fine silt. Along the north-to-south direction, the levee sections included four patterns from the crown to the bottom (see Figure 3). The first pattern (medium silt, fine silt, and medium silt) predominated in levee sections 42–40 lkm, 36 lkm, 34 lkm, and 17 lkm, while the second pattern (medium silt and fine silt) predominated in levee sections 38 lkm, 33 lkm, 24–19 lkm, and 16–15 lkm. The third pattern (fine silt, medium silt, and fine silt) only predominated in the 37 lkm and 13 lkm levee sections, while the fourth pattern (fine silt and medium silt) was mainly found in levee sections 35 lkm, 32–28 lkm, 18 lkm, and 14 lkm. Meanwhile, the transverse profiles measured on the Tisza levee included a composition of fine and medium silts in both the river and protected sides (see Figure 4I).

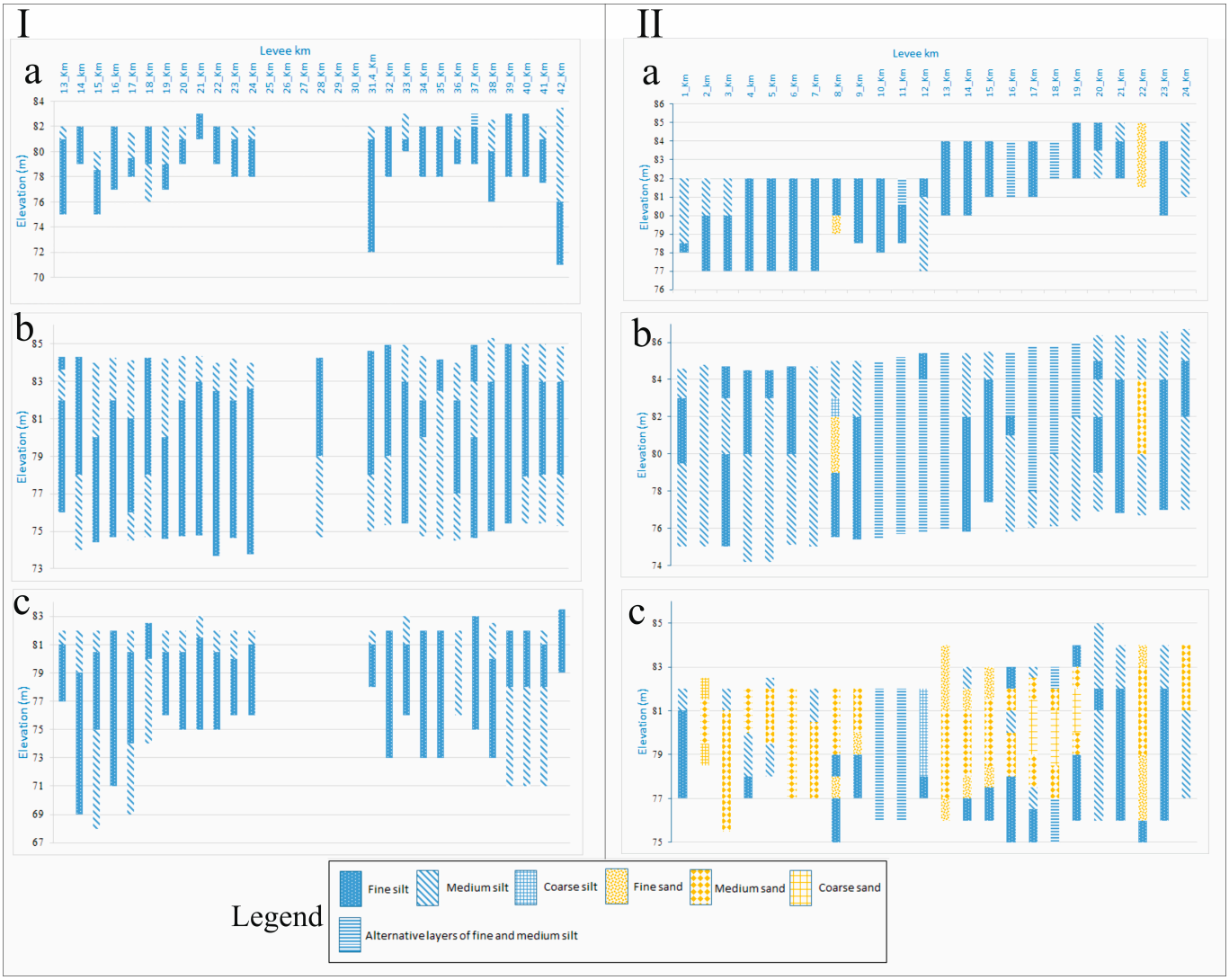


Figure 4. Spatial distribution of levee materials along the investigated sections of the (**I**) Tisza River and (**II**) Maros River levees. Panels show material composition mapped from integrated ERT and sedimentological data: (**a**) riverside slope, (**b**) levee crown, and (**c**) protected side. The mapping illustrates the lateral and vertical variability of sediment types that control seepage behavior and levee stability.

In contrast to the Tisza levee section, the Maros levee section contained materials of all sizes, ranging from fine silt to coarse sand (i.e., fine silt, medium silt, coarse silt, fine sand, medium sand, and coarse sand), along with alternating fine and medium silts in

several locations. Overall, the longitudinal profiles measured on the crown of the Maros levee revealed medium and fine silts in the levee core, except in three lkm sections (from east to west) at 8 lkm, 16 lkm, and 22 lkm, with compositions of coarse silt, fine sand, and medium sand. From the crown to the bottom, the levee sections revealed five patterns: (1) a pattern of medium and fine silts predominating in levee sections 24 lkm, 20 lkm, and 1 lkm; (2) a pattern of medium and fine silts predominating in levee sections 23 lkm, 21 lkm, 15 lkm, and 9 lkm; (3) a pattern of alternating medium and fine silts in the same unit predominating in levee sections 19–16 lkm and 13–10 lkm; (4) a pattern of fine and medium silts predominating in levee sections 14 lkm and 6–3 lkm; and (5) a pattern of medium silt predominating in levee sections 15 lkm, 7 lkm, and 2 lkm. As for the transverse profiles of the Maros levee, 17 lkm sections (2–9 lkm, 13–19 lkm, 22 lkm, and 24 lkm) among all of the investigated sections (of 24 lkm length) showed a sand backfill on the protected side. The remaining sections contained silty materials, while the riverside of the Maros levee exhibited a silty composition (see Figure 4II) [40].

It should be noted that the spatial distribution of levee materials between ERT profiles and borehole locations represents an interpretation constrained by the available measurements; therefore, some uncertainty remains in the interpolated zones between survey points.

4.3. Sedimentological Analysis

A total of 220 samples were collected at 0.4-m depth intervals for W analyses. These samples were sorted into seven categories of grain size in order to investigate the dominant compositions of the Tisza and Maros levees. The analysis showed that fine silt predominantly formed the bodies of both levee systems (55.6%), followed by medium silt (31.2%), medium sand (6.3%), and coarse silt (4.5%). The other classes (very fine silt, fine sand, and coarse sand) represented a minor proportion, between 0.4% and 1.3%. Collectively, the fine-grained materials (fine and medium silts) comprised 87% of the levee bodies, indicating that the materials of both levees offer good flood protection.

4.3.1. Classification of Levee Materials

The analysis revealed that the specific resistivity of the levee sediments varied considerably with W, and distinct resistivity ranges were determined for each material type based on the ERT measurements. The water content of all samples was measured, then the borehole samples were classified into seven sedimentary classes according to their D50 values as follows: (1) fine silt characterized by D50 = 11–14 μm, W = 16–24%, and R = 15–39 Ωm (average: 24 Ωm; standard deviation: 86); (2) medium silt characterized by D50 = 16–19 μm, W = 11–22%, and R = 25–63 Ωm (average: 34 Ωm; standard deviation: 191); (3) coarse silt characterized by D50 = 34–38 μm, W = 12–16%, and R = 90–128 Ωm (average: 97 Ωm; standard deviation: 116); (4) fine sand characterized by D50 = 109–164 μm, W = 4–7%, and R = 108–199 Ωm (average: 173 Ωm; standard deviation: 93); (5) medium sand characterized by D50 = 332–430 μm, W = 3–5%, and R = 276–798 Ωm (average: 518 Ωm; standard deviation: 525). Two additional classes were identified in one drilling sample from the levee foot of a 16 lkm section in the Maros levee: (6) very fine silt characterized by D50 = 6.5 μm, W = 22.7%, and R = 13.5 Ωm; and (7) coarse sand (D50 = 582 μm, W = 2.2%, and R = 3095 Ωm). The main classes are presented in Figure 5 [40]. In the boxplots, the colored dots represent statistical outliers (individual observations that fall outside the range for each sediment class).

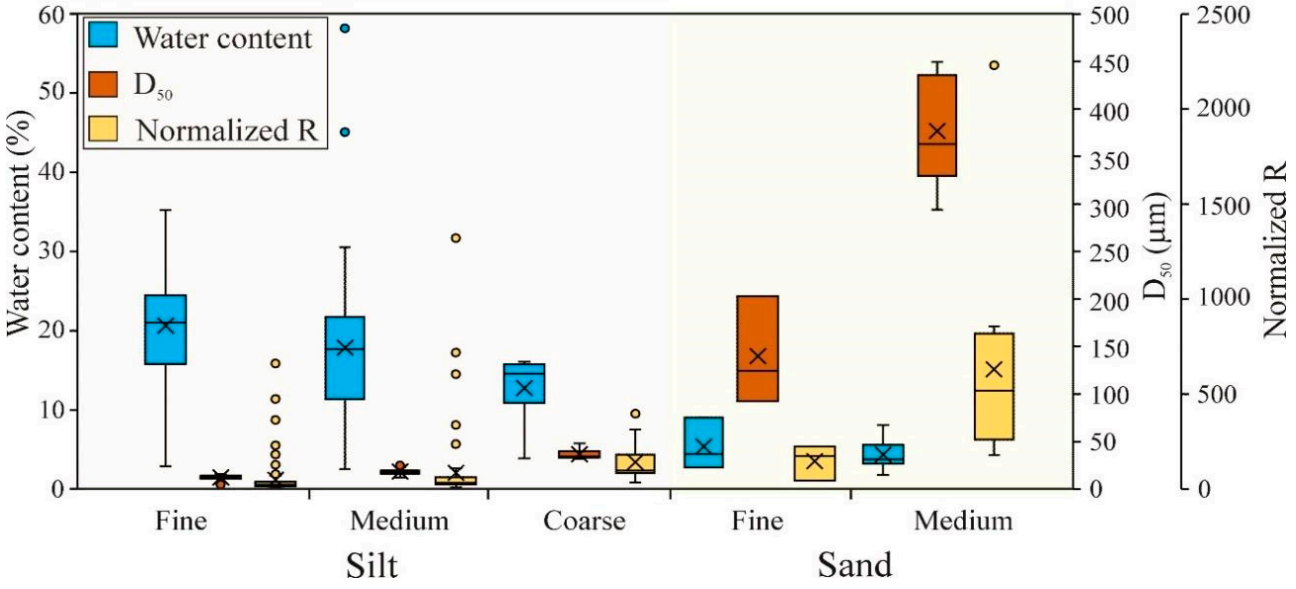


Figure 5. Classification of levee materials from the Tisza and Maros sections based on D_{50}, W, and R of the investigated samples. The diagram illustrates the relationships among these parameters and their role in distinguishing sediment classes with differing hydraulic and geotechnical properties.

4.3.2. Relationships Among the R, D50, and W of the Levee Materials

For the samples in each borehole drilled on the Tisza and Maros levees, the Pearson and Spearman correlations of R vs. W and R vs. D50 were computed by using SPSS software. Based on the findings, R was non-linearly related to both D50 and W, but a nearly monotonic relationship was also observed. Although Pearson's coefficient explained the R vs. W correlation with a higher degree of significance than Spearman's coefficient, the R vs. D50 correlation was better explained by Spearman's coefficient (See Table A2 in Appendix A) at some individual boreholes. In many instances, the R, W, and D50 were uncorrelated in individual boreholes.

Since the correlations between R and D50 and between R and W in individual boreholes were in general weak and differed from those among all of the samples, we turned to develop a classification method to classify all the samples into three classes depending on W: Class 1, in the W range of 0–10%; Class 2, in the W range of 11–20%; and Class 3, in the W range of 21–30% or higher then analyzed the relation between R and D50. The Pearson correlation results were high (0.672), moderate (0.574), and negligible (0.213) for the three classes, respectively. Meanwhile, R was significantly positively correlated with D50, with the highest degree of significance in Classes 1 and 2 of the W samples (0.01). This result might explain the effect of the classification method of W on the relationship between R and D50 (i.e., increasing W reduces the strength of the relationship between R and D50, as observed in Class 3 of the W samples) and the high degrees of significance among these parameters only emerged when all of the samples were combined. These results indicate that drier sections of the levees show a strong positive correlation between resistivity and grain size, whereas at higher moisture contents this relationship breaks down. Physically, this is expected: when W > ~20%, the pore water dominates the electrical conduction, masking the influence of grain-size distribution. In contrast, in low-W conditions, coarser grains (larger D50) lead to higher resistivity due to lower surface area and reduced clay content.

4.3.3. Relationships Between R and Other Physical Parameters

Further information on the levee materials of the Tisza and Maros Rivers was obtained from the relationships between R and other parameters, such as K, φ, and ρ, in the 49 samples. Based on their K values, the levee compositions were classified into aquitard and non-aquitard materials. In this regard, 16 out of the 21 samples collected from the Tisza levee and 19 out of the 29 samples collected from the Maros levee exhibited an aquitard nature, indicating that the levee materials are capable of restricting water flow. Therefore, the condition of the investigated levees is considered good in terms of flood protection (see Table A1 in Appendix A). Additionally, the correlations between R and other parameters, such as W, D50, K, φ, and ρ, of the levee materials were done by Spearman coefficient. Among the 49 samples, R and W were weakly negatively correlated (−0.378) with a high significance level (0.007), while R was moderately positively correlated with D50 (0.571), positively correlated with K (0.374) and φ (0.34), and negatively correlated with ρ (−0.35). These trends suggest that higher resistivity tends to associate with coarser, more porous materials: R increases with larger grain size D50, higher hydraulic conductivity K, and greater porosity φ, while R decreases with higher moisture content W and bulk density ρ. This aligns with geophysical expectations, as fine-grained, dense, and moist soils conduct electricity more readily. The negative R–W correlation confirms that moisture reduces resistivity, and the positive R–D50 correlation (especially when controlling for W) indicates coarser grains yield higher resistivity. These correlations reinforce our interpretation of ERT profiles in terms of levee material properties.

4.4. Prediction of D50 Using ML Models

The performance of the tested four ML models in predicting D50 from R and W were compared (see Table 1) and the results reveal that the RFR outperforms others, achieving the highest R^2 on both training (0.978) and test (0.81) sets, the lowest test RMSE (53.9), and a reasonable MAPE (41.9%). This demonstrates its superior ability to capture complex, non-linear patterns in the data with minimal overfitting. On the other hand, LR emerges as the worst-performing model, with an R^2 of only 0.66 on the test set and a high MAPE (124%), indicating its limited capacity to model non-linear relationships. While ANN and SVR offer moderate performance, their generalization ability is hindered, as seen in ANN's excessively high MAPE (238.23%) and SVR's test RMSE (71.3) (Figure 6). Notably, the ANN achieved high accuracy on training data but its test error (e.g., MAPE) was much larger, suggesting some overfitting. We mitigated this via regularization and dropout, but the limited dataset likely constrained ANN's generalization.

Table 1. The statistical parameters used to assess the ML models.

Model	R^2 (Train)	R^2 (Test)	RMSE (Train)	RMSE (Test)	MAPE (%) (Train)	MAPE (%) (Test)	MEDAE (Train)	MEDAE (Test)	MAE (Train)	MAE (Test)
RFR	0.978	0.81	11.765	53.9	16.788	41.9	1.246	4.6	4.715	20
ANN	0.968	0.74	13.98	62.49	166.8	238.23	2.73	3.26	6.22	18.06
LR	0.79	0.66	36	71	97	124	9	13	20	34.9
SVR	0.8	0.66	35	71.3	24	51	2	3.71	10	25.48

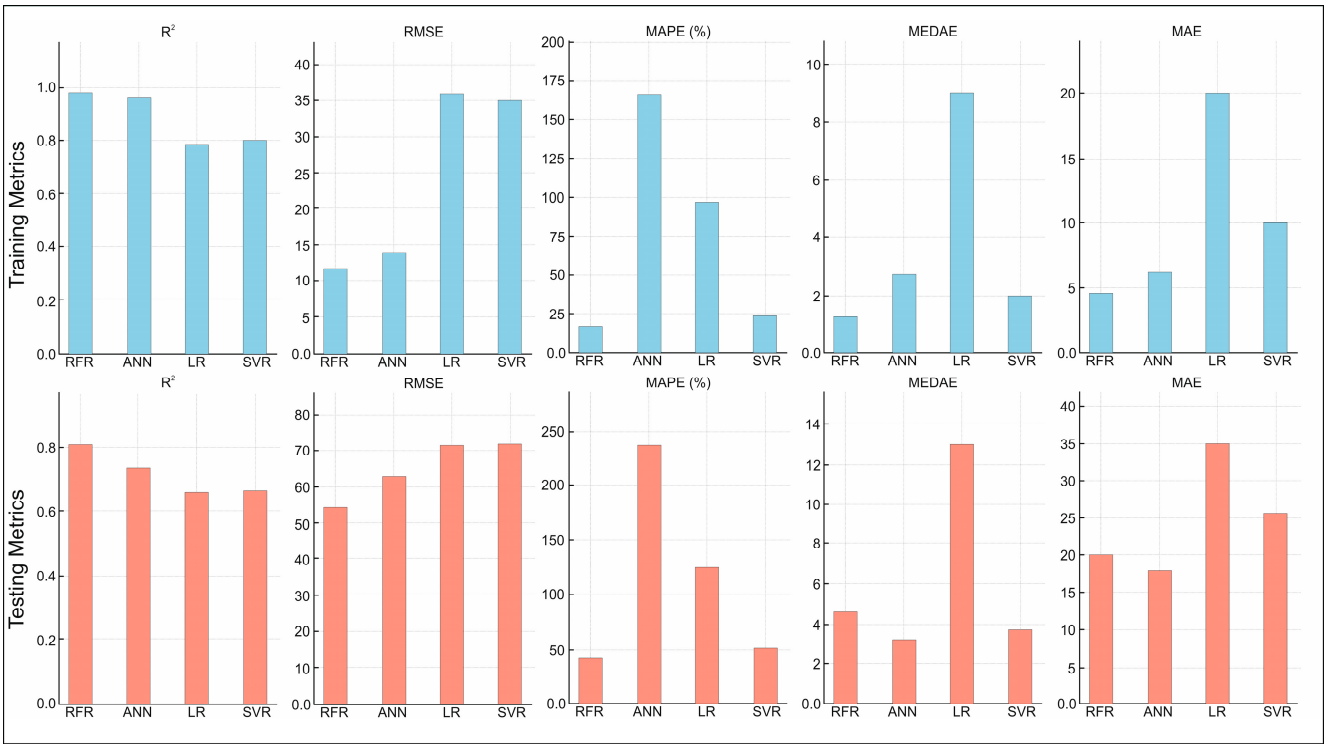


Figure 6. Comparison of statistical metrics for different models (RFR, ANN, LR, SVR) based on training and testing datasets. The upper row represents the metrics for training data, and the lower row represents the metrics for testing data. Each column shows a specific metric: R^2, RMSE, MAPE (%), MEDAE, and MAE. Bars are dynamically scaled to highlight the differences across models for each metric.

5. Discussion

5.1. Flood-Safety Implications of Levee Composition

The geophysical and sedimentological characterization of the levees provides direct insights into their hydraulic performance and flood-safety condition. Consistent with previous findings by [13,14], our results confirm that levees composed predominantly of fine-grained, cohesive materials exhibit lower permeability and better resistance to internal erosion. The Tisza levee is dominated by fine silts forming a continuous, low-permeability core—an aquitard structure that effectively reduces seepage during high-water events. Similar relationships between fine-grained composition and seepage control were reported by [17,18] in alluvial levees of comparable texture.

In contrast, the Maros levee shows pronounced heterogeneity, with alternating silt and sand units—particularly sand lenses on the protected side—that interrupt the continuity of the fine-silt matrix. These coarse-grained lenses correspond to the highest resistivity anomalies detected in the ERT profiles (up to 3025 Ωm), reflecting the lower moisture retention and higher permeability of sandy materials. This configuration increases the potential for preferential flow paths, aligned with the results of Borgatti et al. [19] and Crawford and Bryson [21], who linked coarse inclusions within levee cores to elevated internal-erosion risk. Our ERT-based classification aligns with the interpretations of [6,23], showing that fine-silt-dominated levees (like the Tisza) correspond to low or moderate risk levels, whereas sections containing coarse-grained units (e.g., Maros lkm 8, 16, and 22) reach high-risk conditions due to higher hydraulic conductivity and discontinuous fine covers.

The number of structural layers also exerts a major control on stability. Levees with fewer internal units and uniform composition tend to perform better under prolonged

saturation, as homogeneous fine-silt cores limit internal pressure gradients and are easier to maintain. The Tisza levee, characterized by a single dominant fine-silt unit with minor medium-silt interbeds, therefore represents a relatively stable structure. In contrast, the Maros levee, composed of up to six layers with alternating textures at many parts, exhibits multiple interfaces susceptible to seepage and deformation. This observation supports Galli [7] and Schweitzer [8], who emphasized that complex, multi-layered embankments are inherently more vulnerable and require detailed geophysical monitoring to detect hidden weaknesses.

From a practical perspective, integrating compositional mapping with flood-risk management enables targeted maintenance and emergency planning. Sections where fine-silt continuity is interrupted—particularly where medium silt reaches the riverside surface—should be prioritized for reinforcement using impervious clay blankets, cutoff walls, or slurry barriers to reduce seepage potential [59]. In the Maros levee, zones containing sand backfill on the protected side likely function as drainage layers intended to dissipate pore pressures during drawdown; however, these must be coupled with proper filter protection to prevent soil loss and internal erosion.

5.2. Comparative Performance of ML Algorithms in Geotechnical Prediction

Our comparative modeling confirms the value of ML algorithms for predicting geotechnical parameters from geophysical data and indicates the applicability of the tested models in predicting D50 from R and W.

Although D50 is an intrinsic sedimentological property, it is treated here as an inferred parameter rather than a causally dependent variable. Electrical resistivity and water content do not modify grain size but act as physically meaningful proxies that respond to grain-size-controlled pore structure and hydraulic behavior, allowing D50 to be estimated statistically without implying causation.

The RFR achieved the highest accuracy and generalization in predicting D50, outperforming both linear and more complex non-linear models such as ANN and SVR. This result aligns with Kundu et al. [37] and Hamada et al. [35], who emphasized that ensemble tree-based methods capture non-linear interactions effectively while resisting overfitting. The RFR's bagging structure allowed it to model the subtle interplay between R, W, and D50 even with limited data, similar to the findings of [32,34].

The ANN, despite its capacity for complex non-linear learning [31,33], exhibited overfitting—likely due to the modest dataset size—mirroring observations by [34] regarding deep models' data dependency. The SVR performed moderately, comparable to the results of [36], suggesting that once moisture classes were accounted for, the R–D50 relationship remained largely monotonic.

Importantly, the RFR also offered interpretability—identifying resistivity as the dominant predictor—making it well-suited for practical, physically consistent levee characterization. This represents a methodological advantage over black-box models, as it preserves a direct link between geophysical measurements and geotechnical meaning. Thus, ensemble tree-based models provide the most balanced combination of accuracy, stability, and explainability for coupling geophysical and geotechnical datasets in levee investigations.

This study contributes to a refined understanding of how resistivity data can be interpreted in terms of levee material characteristics, especially grain size distribution and moisture content. Rather than treating resistivity anomalies qualitatively, this work formalizes their quantitative meaning in a geotechnical context. We found that absolute resistivity values, when contextualized by the current moisture regime, can serve as reliable indicators of material type.

5.3. Relevance of the Results for Water Management Applications

The integrated ERT and ML approach developed in this study has significant implications for levee maintenance programs and long-term monitoring strategies. Traditionally, levee assessments rely on periodic visual inspections and sparse borehole drillings, which may miss subsurface anomalies until they manifest as structural anomalies and flood phenomena (e.g., seepage boils or slumps). Our results demonstrate that the proposed method addresses this limitation by providing continuous subsurface information at the scale relevant for flood defense. Non-destructive geophysical surveys, interpreted with the aid of ML, can rapidly map levee composition along extensive lengths, identifying zones of concern without extensive drilling.

For instance, our mapping of the Maros levee pinpointed segments with potential sand inclusions (which could be linked to historical repairs or foundation heterogeneities), indicating priority segments for closer inspection. The developed risk-level mapping can support engineers in developing a maintenance schedule that focuses on moderate- and high-risk sections. Moderate-risk areas may require more frequent geophysical re-surveys or targeted trenching, while high-risk areas could be prioritized for preemptive reinforcement (such as adding a clay core or installing sheet-pile cut-offs).

Moreover, the correlations we established between resistivity and geotechnical parameters (porosity, density, hydraulic conductivity) suggest that ERT monitoring can serve as a proxy for certain physical inspections aligned with other studies [6,12,23,60,61]. This strengthens the scientific justification for integrating geophysics into routine levee monitoring rather than using it solely as a diagnostic tool after failure symptoms appear.

The results of this investigation directly enhance hydrological risk assessments by refining how the probability and consequences of levee failure are estimated under varying flood conditions. Traditional fragility or breach models often assume homogeneous levee properties, yet parameters such as permeability, cohesion, and internal structure are spatially variable. By providing spatially resolved, physically grounded input parameters, this study improves the reliability and predictive capability of such models, aligning with recent advances in spatially explicit flood-risk modeling [62,63].

6. Conclusions

This study combined electrical resistivity tomography (ERT) and borehole sedimentological data to investigate the internal structure and material composition of two river levee sections with complex stratigraphy and flood-related stability concerns. The integration of geophysical and drilling data enabled detailed characterization of levee materials and revealed significant structural heterogeneity within the investigated sections. The results demonstrate that levee materials can be effectively distinguished based on their electrical resistivity, with fine-grained sediments exhibiting lower resistivity values and coarse-grained materials—particularly sand lenses located on the protected side of the levee—showing significantly higher resistivity anomalies. Although the levee cores of the Tisza and Maros sections display broadly similar resistivity ranges and material compositions, notable variability was observed in the relationships among the physical parameters measured in individual boreholes.

A key contribution of this study is the integration of field geophysics with machine-learning techniques to predict geotechnical parameters from geophysical data. Among the tested algorithms, RFR proved to be the most robust and accurate model for predicting median D50 using R and W as predictors. These findings demonstrate that resistivity measurements, when interpreted in the context of moisture conditions, can serve as reliable indicators of levee material properties. The results further highlight the potential of combining physically based geophysical measurements with data-driven mod-

els to construct spatially heterogeneous geotechnical models that better represent real subsurface conditions.

From an engineering perspective, the results emphasize that levees dominated by fine-grained materials with relatively homogeneous internal structures generally exhibit lower seepage risk, whereas levee sections containing coarse-grained sand lenses may create preferential seepage pathways that increase the susceptibility to internal erosion and piping during flood events. In the investigated sections, the presence of coarse sediments on the protected side of the levee may facilitate drainage of infiltrating water during flood conditions; however, discontinuities in the fine-grained cover layers on the riverside slope may locally increase seepage risk.

Nevertheless, several limitations should be acknowledged. The spatial density of borehole observations remains limited relative to the investigated levee lengths, and electrical resistivity measurements are inherently influenced by environmental conditions such as soil moisture and temperature. These factors may introduce uncertainties in the interpretation of geophysical anomalies and the performance of the machine-learning models.

Future research could improve the robustness of levee assessments by incorporating additional borehole data, time-lapse geophysical monitoring, and larger training datasets for machine-learning models. In addition, validating the developed models using independent datasets from other levee sections or different river systems would further demonstrate their generalizability and practical applicability. Expanding this integrated approach to other levee systems would further improve our understanding of levee heterogeneity and its role in flood-risk management.

Overall, the integrated ERT–borehole–machine learning framework presented in this study provides a promising methodology for levee characterization, monitoring, and flood-risk assessment, and may serve as a reference for future investigations of levee systems along major rivers worldwide.

Author Contributions: D.S. and G.S. conceived and designed the study. D.S., E.A., D.F. and G.M. conducted the field investigations, including ERT surveys, sampling, and laboratory analyses. D.S., G.M., V.B.-V. and S.H. contributed to data processing, GIS analysis, and visualization. A.H., A.O. and C.T. assisted with geological interpretation and regional context analysis. D.S., A.M. and A.M.A. developed and implemented the machine learning models and statistical evaluation. T.B. and P.K. supported the data acquisition logistics and geotechnical parameter calibration. D.S. prepared the original draft of the manuscript, and G.S. supervised the research and revised the final version. All authors have read and agreed to the published version of the manuscript.

Funding: The publication was financially supported by the University of Szeged Open Access Fund, Grant ID: 8530. This research was supported by the Interreg VI-A IPA Hungary-Serbia Programme under the project HUSRB/23R/11/006 ADAPTISA.

Data Availability Statement: The data presented in this study are available from the corresponding author upon reasonable request. Due to the sensitive nature of the datasets, which were collected on flood-protection levees, public access is restricted. Data sharing requires permission from the competent water management authority responsible for the levee system.

Acknowledgments: We acknowledge Szabolcs Gáti for contributing to the ERT measurements, and Istvan Fekete for assisting with the laboratory measurements. Special thanks are due to Károly Barta, who guided the borehole sample analysis.

Conflicts of Interest: There are no conflicts of interest to declare.

Appendix A

Table A1. Properties of 49 samples collected from 10 different boreholes.

	Sample ID	lkm (km)	d (cm)	W (%)	D50 (μm)	φ (m/m%)	ρ (g/cm^3)	K (mm/h)	M	R (Ω m)
Tisza levee crown	1	13	270	16.5	18.8	38	1.63	0.007	aquitard	57.2
	2	13	290	16.0	18	39	1.62	0.007	aquitard	43.7
	3	13	300	15.0	16	40	1.59	0.008	aquitard	30.3
	4	13	310	15.0	15.5	36	1.69	0.007	aquitard	24.8
	5	13	570	27.0	14	45	1.47	0.007	aquitard	10.6
	6	13	580	28.0	13.4	44	1.49	0.006	aquitard	10.7
	7	18	300	24.0	12.9	44	1.49	0.006	aquitard	11.9
	8	18	310	24.0	13	35	1.71	0.007	aquitard	12
	9	18	390	22.5	7.5	41	1.56	-	-	12.3
	10	18	510	25.0	12.9	45	1.47	-	-	13
	11	18	520	26.0	12.6	41	1.57	0.007	aquitard	13.2
	12	31.4	150	15.5	12	39	1.63	0.011	aquitard	20.6
	13	31.4	160	16.0	11.9	36	1.69		-	17.5
	14	31.4	250	24.0	10.8	38	1.63	0.012	aquitard	10.9
	15	31.4	410	20.0	12.5	44	1.50	0.015	aquitard	9.7
	16	31.4	420	19.5	13	43	1.51	0.013	aquitard	9.9
	17	37	50	8.0	19.5	38	1.64	24.942	not aquitard	22.7
	18	37	60	9.0	21.4	41	1.57	24.375	not aquitard	20
	19	37	270	12.5	16	35	1.72	0.012	aquitard	8.9
	20	37	270	12.5	16	35	1.72	0.011	aquitard	8.8
	21	37	470	20.0	13.8	-	-	0.012	aquitard	10
Maros levee crown	22	3	150	22.0	17.7	44	1.49	3.487	not aquitard	14.7
	23	3	160	22.0	18.7	50	1.31	0.956	not aquitard	14.5
	24	3	290	21.0	13.5	41	1.55	0.013	aquitard	17.45
	25	3	610	33.5	11.7	-	-	-	-	23.7
	26	3	620	34.0	11.9	46	1.43	0.492	not aquitard	23.7
	30	8	190	14.0	33.6	40	1.58	1.246	not aquitard	92

Table A1. *Cont.*

	Sample ID	lkm (km)	d (cm)	W (%)	D50 (μm)	φ (m/m%)	ρ (g/cm^3)	K (mm/h)	M	R (Ω m)
Maros levee crown	31	8	200	14.0	34.1	42	1.55	0.266	not aquitard	100.2
	32	8	280	3.0	203.1	48	1.38	0.764	not aquitard	168.2
	33	8	420	18.0	15.8	43	1.50	-	-	233
	34	8	490	23.0	13.3	36	1.69	0.012	not aquitard	217
	35	10	150	27.5	20.8	45	1.46	0.113	not aquitard	24.8
	36	10	160	28.0	21.1	48	1.37	0.013	aquitard	25
	37	10	300	21.0	24.2	48	1.37	0.048	not aquitard	28
	38	10	500	17.5	15.7	47	1.39	0.066	not aquitard	31.6
	39	10	510	17.0	15.6	43	1.50	0.012	aquitard	31.8
	40	16	240	11.0	20.5	48	1.38	-	-	88
	41	16	250	12.5	19	45	1.47	0.011	aquitard	85.11
	42	16	250	12.5	19	48	1.37	1.034	not aquitard	85.11
	43	16	470	21.0	15.7	51	1.3	0.010	aquitard	39
	44	16	480	21.0	15.2	46	1.42	0.688	not aquitard	41
	45	20	250	15.0	15	44	1.49	-	-	34.8
	46	20	250	15.0	15	48	1.39	0.113	not aquitard	34.8
	47	20	260	16.0	15.3	45	1.46	0.200	not aquitard	33
	48	20	430	21.0	18.3	41	1.57	0.113	not aquitard	20
	49	20	440	21.0	18.6	45	1.44	0.036	not aquitard	19
Maros protected side	27	3	150	4.0	339.3	47	1.41	525	not aquitard	442
	28	3	160	4.0	331.8	45	1.44	287	not aquitard	606
	29	3	285	27.0	18.8	46	1.43	0.052	not aquitard	1292

Note: d: depth; M: material type.

Table A2. Correlations and degrees of significance between true resistivity and moisture content and between true resistivity and grain size (D50) in the samples at each borehole location on the Tisza and Maros levees.

BH	N/BH	R vs. W by Pearson	Significance	R vs. W by Spearman	Significance	R vs. D50 by Pearson	Significance	R vs. D50 by Spearman	Significance
BH-1	16	−0.269	0.314	−0.424	0.101	0.466	0.069	0.649 **	0.007
BH-2	10	−0.934 **	0.01	−0.842 **	0.002	0.471	0.169	0.195	0.59
BH-3	15	0.332	0.226	0.382	0.16	0.263	0.344	0.422	0.117
BH-4	10	−0.452	0.19	−0.527	0.117	0.416	0.232	0.333	0.347
BH-5	15	−0.217	0.438	−0.233	0.404	0.056	0.842	0.025	0.929
BH-6	10	−0.765 **	0.01	−0.733 *	0.016	0.601	0.066	0.857 **	0.002
BH-7	15	−0.127	0.653	0.034	0.904	0.099	0.725	−0.093	0.742
BH-8	10	0.268	0.454	0.281	0.431	−0.413	0.236	−0.309	0.385
BH-9	17	−0.368	0.146	−0.212	0.414	0.182	0.484	0.153	0.557
BH-10	7	0.782 *	0.038	0.556	0.195	−0.417	0.352	−0.143	0.76
BH-11	17	−0.067	0.797	−0.039	0.881	0.191	0.463	−0.078	0.765
BH-12	11	0.031	0.927	0.2	0.555	0.194	0.567	0.327	0.326
BH-13	15	0.389	0.152	0.356	0.193	−0.083	0.768	−0.014	0.96
BH-14	7	0.582	0.17	0.667	0.102	0.491	0.263	0.36	0.427
BH-15	15	−0.893 **	0.01	−0.924 **	0.01	0.638 *	0.01	0.704 **	0.003
BH-16	7	0.677	0.095	0.714	0.071	−0.165	0.724	0.036	0.939
BH-17	5	−0.869	0.056	−0.6	0.285	0.952 *	0.012	0.900 *	0.037
BH-18	15	−0.776 **	0.001	−0.941 **	0.01	0.800 **	0.01	0.639 *	0.01
BH-19	7	−0.295	0.521	−0.214	0.645	0.655	0.11	0.357	0.432

Note: Number of samples/borehole: N/BH. * and ** denote statistically significant correlations at the $p < 0.05$ and $p < 0.01$ levels, respectively, based on two-tailed tests.

References

1. Mezősi, G. *Natural Hazards and the Mitigation of Their Impacts*; Springer International Publishing AG: Cham, Switzerland, 2022; p. 260. [CrossRef]
2. Ahadiyan, J.; Bahmanpouri, F.; Adeli, A.; Gualtieri, C.; Khoshkonesh, A. Riprap Effect on Hydraulic Fracturing Process of Cohesive and Non-cohesive Protective Levees. *Water Resour. Manag.* **2022**, *36*, 625–639. [CrossRef]
3. Szűcs, P.; Nagy, L.; Ficsor, J.; Kovács, S.; Szlávik, L.; Tóth, F.; Keve, G.; Lovas, A.; Padányi, J.; Balatonyi, L.; et al. Árvízvédelmi ismeretek = Flood Protection. 2019. Available online: http://hdl.handle.net/20.500.12944/13490 (accessed on 15 April 2022). (In Hungarian)
4. Knox, R.L.; Morrison, R.R.; Wohl, E.E. Identification of artificial levees in the contiguous United States. *Water Resour. Res.* **2022**, *58*, e2021WR031308. [CrossRef]
5. Tobin, G.A. The levee love affair: A stormy relationship? *JAWRA J. Am. Water Resour. Assoc.* **1995**, *31*, 359–367. [CrossRef]
6. Sheishah, D.; Kiss, T.; Borza, T.; Fiala, K.; Kozák, P.; Abdelsamei, E.; Tóth, C.; Grenerczy, G.; Páll, D.G.; Sipos, G. Mapping subsurface defects and surface deformation along the artificial levee of the Lower Tisza River, Hungary. *Nat. Hazards J.* **2023**, *117*, 1647–1671. [CrossRef]
7. Galli, L. *Az Árvízvédelmi Földművek Állékonyságának Vizsgálata*; Országos Vízügyi Hivatal: Budapest, Hungary, 1976. Available online: https://library.hungaricana.hu/hu/view/VizugyiKonyvek_078/?pg=57&layout=s (accessed on 20 April 2024). (In Hungarian)
8. Schweitzer, F. Pleisztocen. In *Pannon Enciklopédia: Kertek, Budapest*; Karátson, D., Ed.; Kertek Kiadó: Budapest, Hungary, 2002; pp. 130–135. Available online: https://docplayer.hu/1721975-A-magyarorszagi-folyoszabalyozasok-geomorfologiai-vonatkozasai.html (accessed on 20 May 2023).
9. Amissah, G.J.; Kiss, T.; Fiala, K. Morphological evolution of the Lower Tisza River (Hungary) in the 20th century in response to human interventions. *Water* **2018**, *10*, 884. [CrossRef]
10. Kovács, D. *Árvízvédelem, Folyó-és Tószabályozás, Víziutak Magyarországon (Flood Control, Regulation of Rivers and Lakes and Waterways in Hungary)*; National Water Management Authority (OVH): Budapest, Hungary, 1979.

11. Tímár, A. Árvízvédelmi töltések potenciális veszélyforrásai a Körösök vidékén= Potential Sources of Danger of Flood Protection Dams in the Körös River Area. *Hadmérnök* **2020**, *15*, 107–119. [CrossRef]
12. Sheishah, D.; Sipos, G.; Hegyi, A.; Kozák, P.; Abdelsamei, E.; Tóth, C.; Onaca, A.; Páll, D.G. Assessing the Structure and Composition of Artificial Levees Along the Lower Tisza River (Hungary). *Geogr. Pannonica* **2022**, *26*, 258–272. [CrossRef]
13. Asch, T.H.; Deszcz-Pan, M.; Burton, B.L.; Ball, L.B. *Geophysical Characterisation of American River Levees, Sacramento, California, Using Electromagnetics, Capacitively Coupled Resistivity, and DC Resistivity*; USGS Open File Report (2008-1109); USGS: Reston, VA, USA, 2008; 12p. Available online: https://pubs.usgs.gov/of/2008/1109/index.html (accessed on 15 May 2023).
14. Di Prinzio, M.; Bittelli, M.; Castellarin, A.; Pisa, P.R. Application of GPR to the monitoring of river embankments. *J. Appl. Geophys.* **2010**, *71*, 53–61. [CrossRef]
15. Hibert, C.; Grandjean, G.; Bitri, A.; Travelletti, J.; Malet, J.-P. Characterising landslides through geophysical data fusion: Example of the La Valette landslide (France). *Eng. Geol.* **2012**, *128*, 23–29. [CrossRef]
16. Morelli, G.; Francese, R. A fast and integrated geophysical imaging system for large-scale levee monitoring. In *Symposium on the Application of Geophysics to Engineering and Environmental Problems, Denver, CO, USA, 17–21 March 2013*; EEGS: Denver, CO, USA, 2012. [CrossRef]
17. Chlaib, H.K.; Mahdi, H.; Al-Shukri, H.; Su, M.M.; Catakli, A.; Abd, N. Using ground-penetrating radar in levee assessment to detect small-scale animal burrows. *J. Appl. Geophys.* **2014**, *103*, 121–131. [CrossRef]
18. Busato, L.; Boaga, J.; Peruzzo, L.; Himi, M.; Cola, S.; Bersan, S.; Cassiani, G. Combined geophysical surveys for the characterization of a reconstructed river embankment. *Eng. Geol.* **2016**, *211*, 74–84. [CrossRef]
19. Borgatti, L.; Forte, E.; Mocnik, A.; Zambrini, R.; Cervi, F.; Martinucci, D.; Zamariolo, A. Detection and characterization of animal burrows within river embankments utilizing coupled remote sensing and geophysical techniques: Lessons from River Panaro (northern Italy). *Eng. Geol.* **2017**, *226*, 277–289. [CrossRef]
20. Bakula, K.; Salach, A.; Wziątek, D.Z.; Ostrowski, W.; Górski, K.; Kurczyński, Z. Evaluation of the accuracy of lidar data acquired using a UAS for levee monitoring: Preliminary results. *Int. J. Remote Sens.* **2017**, *38*, 2921–2937. [CrossRef]
21. Crawford, M.M.; Bryson, L.S. Assessment of active landslides using field electrical measurements. *Eng. Geol.* **2018**, *233*, 146–159. [CrossRef]
22. Sheishah, D.; Sipos, G.; Barta, K.; Abdelsamei, E.; Hegyi, A.; Onaca, A.; Abbas, A.M. Comparative evaluation of the material of the artificial levees. *J. Environ. Geogr.* **2023**, *16*, 12615. [CrossRef]
23. Abdelsamei, E.; Tímár, A.; Sheishah, D.; Blanka-Végi, V.; Hegyi, A.; Runa, B.; Balogh, O.; Ali, A.; Sipos, G. Detection of seepage zones in artificial levees: A case study at the Körös River, Hungary. *Open Geosci.* **2024**, *16*, 20220744. [CrossRef]
24. Sentenac, P.; Benes, V.; Budinsky, V.; Keenan, H.; Baron, R. Post flooding damage assessment of earth dams and historical reservoirs using non-invasive geophysical techniques. *J. Appl. Geophys.* **2017**, *146*, 138–148. [CrossRef]
25. Fargier, Y.; Lopes, S.P.; Fauchard, C.; François, D.; Côte, P. DC-Electrical Resistivity Imaging for embankment dike investigation: A 3D extended normalization approach. *J. Appl. Geophys.* **2014**, *103*, 245–256. [CrossRef]
26. Tresoldi, G.; Arosio, D.; Hojat, A.; Longoni, L.; Papini, M.; Zanzi, L. Long-term hydrogeophysical monitoring of the internal conditions of river levees. *Eng. Geol.* **2019**, *259*, 105139. [CrossRef]
27. Perri, M.T.; Boaga, J.; Bersan, S.; Cassiani, G.; Cola, S.; Deiana, R.; Simonini, P.; Patti, S. River embankment characterisation: The joint use of geophysical and geotechnical techniques. *J. Appl. Geophys.* **2014**, *110*, 5–22. [CrossRef]
28. Dezert, T.; Fargier, Y.; Palma Lopes, S.; Côte, P. Geophysical and geotechnical methods for fluvial levee investigation: A review. *Eng. Geol.* **2019**, *260*, 105206. [CrossRef]
29. Jodry, C.; Palma Lopes, S.; Fargier, Y.; Sanchez, M.; Côte, P. 2D-ERT monitoring of soil moisture seasonal behaviour in a river levee: A case study. *J. Appl. Geophys.* **2019**, *167*, 140–151. [CrossRef]
30. Rahimi, S.; Wood, C.M.; Coker, F.; Moody, T.; Bernhardt-Barry, M.; Mofarraj Kouchaki, B. The combined use of MASW and resistivity surveys for levee assessment: A case study of the Melvin Price Reach of the Wood River Levee. *Eng. Geol.* **2018**, *241*, 11–24. [CrossRef]
31. Padhan, M.K.; Rai, A.; Mitra, M. Prediction of grain size distribution in microstructure of polycrystalline materials using one dimensional convolutional neural network (1D-CNN). *Comput. Mater. Sci.* **2023**, *229*, 112416. [CrossRef]
32. Bordas, A.; Zhang, J.; Nino, J.C. Application of deep learning workflow for autonomous grain size analysis. *Molecules* **2022**, *27*, 4826. [CrossRef]
33. Ding, X.; El-Zein, A. Predicting soil water retention curves using machine learning: A study of model architecture and input variables. *Eng. Appl. Artif. Intell.* **2024**, *133*, 108122. [CrossRef]
34. Bordignon, F.; de Figueiredo, L.P.; Exterkoetter, R.; Rodrigues, B.B.; Duarte, M. Deep learning for grain size and porosity distributions estimation on micro-CT images. In Proceedings of the 16th International Congress of the Brazilian Geophysical Society & EXPOGEF, Rio de Janeiro, Brazil, 19–22 August 2019; pp. 1–6.
35. Hamada, G.; Sakka, A.; Nyein, C. Prediction of Porosity and Water Saturation Using Neural Networks in Shaly Sand Reservoirs, Western Deseret, Egypt. *J. Pet. Min. Eng.* **2020**, *22*, 80–91. [CrossRef]

36. Sastre, C.; Benz, M.; Gourvès, R.; Breul, P.; Bacconnet, C. Automatic methodology to predict grain size class from dynamic penetration test using neural networks. In *5th International Conference on Geotechnical and Geological Site Characterization*; ISC: Gold Coast, Australia, 2016; Volume 5, pp. 1465–1470.
37. Kundu, S.K.; Dey, A.K.; Sapkota, S.C.; Debnath, P.; Saha, P.; Ray, A.; Khandelwal, M. Advanced predictive modelling of electrical resistivity for geotechnical and geo-environmental applications using machine learning techniques. *J. Appl. Geophys.* **2024**, *231*, 105557. [CrossRef]
38. Chang, P.Y.; Puntu, J.M.; Lin, D.J.; Amania, H.H.; Chen, W.S.; Lin, A.T.S. Application of machine learning and resistivity measurements for 3D apparent geological modeling in the Yilan plain, Taiwan, at the SW Tip of the Okinawa trough. *Geosci. Lett.* **2024**, *11*, 25. [CrossRef]
39. Kiss, T.; Fiala, K.; Sipos, G.; Szatmári, G. Long-term hydrological changes after various river regulation measures: Are we responsible for flow extremes. *Hydrol. Res.* **2019**, *50*, 417–430. [CrossRef]
40. Sheishah, D. Mapping and Evaluating the Condition of Artificial Levees. Ph.D. Thesis, University of Szeged, Szeged, Hungary, 2023; 127p. Available online: https://doktori.bibl.u-szeged.hu/id/eprint/11801/ (accessed on 10 March 2024).
41. OVF. Árvízi Kockázati Térképezés és Stratégiai Kockázatkezelési terv Készítése (Flood Risk Mapping and Strategic Risk Management Plan), Project Report of the National Water Directorate Hungary. 2014. Available online: http://www.vizugy.hu/vizstrategia/documents/B91A47EC-E3B8-4D58-A15F-3E522958BEE8/Orszagos_elontes_1e_web.pdf (accessed on 15 May 2023).
42. Loke, M.H. *Tutorial: 2-D and 3-D Electrical Imaging Surveys*, Revised ed.; Geotomo Software: Penang, Malaysia, 2004; p. 136.
43. Constable, S.C.; Parker, R.L.; Constable, C.G. Occam's inversion: A practical algorithm for generating smooth models from electromagnetic sounding data. *Geophysics* **1987**, *52*, 289–300. [CrossRef]
44. De Groot-Hedlin, C.; Constable, S. Occam's inversion to generate smooth, two dimensional models from magnetotelluric data. *Geophysics* **1990**, *55*, 1613–1624. [CrossRef]
45. Fetter, C.W. Properties of Aquifers. In *Applied Hydrogeology*; University of Wisconsin: Oshkosh, WI, USA, 2001; 625p. Available online: https://arjzaidi.files.wordpress.com/2015/09/unimasr-com_e7ce669a880a8c4c70b4214641f93a02.pdf (accessed on 20 September 2024).
46. Levesque, R. *SPSS Programming and Data Management: A Guide for SPSS and SAS Users*; SPSS Inc.: Chicago, IL, USA, 2007.
47. Breiman, L. Random forests. *Mach. Learn.* **2001**, *45*, 5–32. [CrossRef]
48. McCulloch, W.S.; Pitts, W.A. logical calculus of the ideas immanent in nervous activity. *Bull. Math. Biophys.* **1943**, *5*, 115–133. [CrossRef]
49. Youshen, X. A new neural network for solving linear and quadratic programming problems. *IEEE Trans. Neural Netw.* **1996**, *7*, 1544–1548. [CrossRef] [PubMed]
50. Mohsen, A.; Kovács, F.; Kiss, T. Remote sensing of sediment discharge in rivers using Sentinel-2 images and machine-learning algorithms. *Hydrology* **2022**, *9*, 88. [CrossRef]
51. Sheishah, D.; Mohsen, A.; Abdelsamei, E.; Babcsányi, I.; Alsenjar, O.; Magyar, G.; Végi, V.B.; Solymos, K.; Sipos, G. Remote sensing-based modeling and mapping of seasonal water quality dynamics in Vadkert Lake, Hungary. *Front. Environ. Sci.* **2025**, *13*, 1665776. [CrossRef]
52. Sheishah, D.; Abdelsamei, E.; Mohsen, A.; Blanka Végi, V.; Kozák, P.; Fiala, K.; Kovács, F.; Babcsányi, I.; Sipos, G. Integrating Ground Penetrating Radar and machine learning for assessment of lake bed permeability and potential vertical-water-loss zones in shallow lake under climatic stress. *EGUsphere* 2025, *preprint*. [CrossRef]
53. Mohsen, A.; Kovács, F.; Baranya, S.; Károlyi, C.; Sheishah, D.; Kiss, T. Insights into suspended sediment and microplastic budget of a lowland river: Integrating in-situ measurements, Sentinel-2 imagery, and machine learning. *Sci. Total Environ.* **2025**, *984*, 179716. [CrossRef] [PubMed]
54. Smola, A.J.; Schölkopf, B. A tutorial on support vector regression. *Stat. Comput.* **2004**, *14*, 199–222. [CrossRef]
55. Hutchings, A.; Hollywood, J.; Lamping, D.L.; Pease, C.T.; Chakravarty, K.; Silverman, B.; Choy, E.H.S.; Scott, D.G.; Hazleman, B.L.; Bourke, B.; et al. Stability prediction of Himalayan residual soil slope using artificial neural network. *Nat. Hazards* **2020**, *103*, 3523–3540. [CrossRef]
56. Bharati, A.K.; Ray, A.; Khandelwal, M.; Rai, R.; Jaiswal, A. Stability evaluation of dump slope using artificial neural network and multiple regression. *Eng. Comput.* **2022**, *38*, 1835–1843. [CrossRef]
57. Paliwal, M.; Goswami, H.; Ray, A.; Bharati, A.K.; Rai, R.; Khandelwal, M. Stability prediction of residual soil and rock slope using artificial neural network. *Adv. Civ. Eng.* **2022**, *2022*, 4121193. [CrossRef]
58. Rathor, S.K.; Mohanta, A.; Patra, K.C. Validation of Computational Fluid Dynamics Approach of Lateral Velocity Profile Due to Curvature Effect on Floodplain Levee of Two-stage Meandering Channel. *Water Resour. Manag.* **2022**, *36*, 5495–5520. [CrossRef]
59. *EM 1110-2-1913*; Engineering and Design—Design and Construction of Levees. Department of the Army, US Army Corps of Engineers: Washington, DC, USA, 2000. Available online: https://www.publications.usace.army.mil/Portals/76/Publications/EngineerManuals/EM_1110-2-1913.pdf (accessed on 13 October 2024).

60. Kearey, P.; Brooks, M.; Hill, I. *An Introduction to Geophysical Exploration*; John Wiley & Sons: Hoboken, NJ, USA; Department of Earth Sciences University of Bristol: Bristol, UK, 2013; 281p. Available online: https://faculty.ksu.edu.sa/sites/default/files/AN_INTRODUCTION_TO_GEOPHYSICAL_EXPLORATION_brooks_0_0.pdf (accessed on 20 April 2025).
61. Ali, A.M.; Timar, A.; Boyd, J.P.; Barta, K.; Abdelsamei, E.; Sheishah, D.; Hegyi, A.; Blanka-Végi, V.; Sipos, G. Quantifying seepage dynamics in a real-scale levee using time-lapse 3D ERT and novel spatiotemporal metrics. *Eng. Geol.* **2025**, *357*, 108386. [CrossRef]
62. D'Oria, M.; Maranzoni, A.; Mazzoleni, M. Probabilistic assessment of flood hazard due to levee breaches using fragility functions. *Water Resour. Res.* **2019**, *55*, 8740–8764. [CrossRef]
63. Mainguenaud, F.; Khan, U.T.; Peyras, L.; Carvajal, C.; Beullac, B.; Sharma, J. Probabilistic flood hazard assessment for multiple flood and levee breaching scenarios: A case study of Etobicoke Creek, Canada. *J. Flood Risk Manag.* **2025**, *18*, e70002. [CrossRef]

Disclaimer/Publisher's Note: The statements, opinions and data contained in all publications are solely those of the individual author(s) and contributor(s) and not of MDPI and/or the editor(s). MDPI and/or the editor(s) disclaim responsibility for any injury to people or property resulting from any ideas, methods, instructions or products referred to in the content.